Type-2 Fuzzy Single Hidden Layer Recurrent Neural Adaptive Terminal Super-Twisting Control of Robot Joint

Xiao Lin, Yu Xia, *Member*, *IEEE*, Zsófia Lendek, *Member*, *IEEE*, Radu-Emil Precup, *Fellow*, *IEEE*, Imre J. Rudas, *Life Fellow*, *IEEE*, and Ramesh K. Agarwal, *Life Fellow*, *IEEE*

***Abstract*—This research proposes a neural network-based super-twisting controller for robot joints. A modified fast non-singular terminal sliding surface is introduced, which not only avoids singularity but also increases the convergence rate of the sliding mode control. To address the challenge of system uncertainty modeling, a type-2 fuzzy single hidden layer recurrent neural network (T2FSHLRNN) is proposed. The T2FSHLRNN, configured as a weighted combination of a type-2 fuzzy neural network and a single hidden layer network, demonstrates strong global learning ability. Leveraging its internal and external double-layer feedback mechanism, the network can incorporate both current and previous error information during the approximation process, effectively improving the approximation accuracy and reducing system chattering. Furthermore, an adaptive gain function is proposed and an adaptive terminal super-twisting controller based on T2FSHLRNN (ATSC-T2FSHLRNN) is developed. The system's stability under unknown disturbance is ensured using Lyapunov synthesis. Based on this, the online parameter learning algorithm for T2FSHLRNN and the variable gains of the ATSC are derived. Simulations confirm the effectiveness of the proposed ATSC-T2FSHLRNN.**

***Index Terms*—Robot joint, super-twisting controller, type-2 fuzzy neural network, unknown disturbance, variable gains.**

I. Introduction

ROBOT joints find extensive applications in diverse fields, including industrial manufacturing, logistics warehousing, medical, service, military defense, education, scientific research, and other fields. High precision control of robot joints is of utmost importance. It is a key factor in enhancing the motion accuracy of robots, strengthening their task-execution capabilities, ensuring stable operation, and promoting intelligent collaborative operations [1], [2]. This research focuses on the control design for robot joints composed of harmonic reducer and motor (RJCHRM).

Traditional control methods for RJCHRM such as PID control [3], [4], backstepping [5], [6], feed-forward [7] and singular perturbation methods [8] can achieve good control performance. However, these methods are suitable for occasions where the servo accuracy requirements are not very high. To attain better dynamic performance of joint modules, PID and robust control were combined to design a model-based robust controller and achieved good results in dealing with system uncertainties [9], [10]. In the Active Disturbance Rejection Control (ADRC) of the joint module designed in [11], the resilience to uncertainties was enhanced through the utilization of a reduced-order state observer. For flexible joint robots equipped with low-precision sensors, [12] proposed an adaptive tracking control scheme. For vibration suppression in elastic joint manipulators, a type-2 fuzzy controller was designed in [13]. A modified sliding mode control (SMC) relying on fuzzy system uncertainty identification was proposed in [14], and was used to improve the precision of electromagnetic torque control. To address the speed fluctuation within the gimbal system, a state observer and SMC-based composite controller was proposed in [15]. [16] and [17] fused type-2 fuzzy systems with SMC for robotic manipulators to enhance adaptability and robustness under uncertainties and faults. To further improve the robustness and tracking performance of robotic manipulators, [18] integrated neural networks with a type-2 fuzzy system into SMC.

Even though the previously mentioned controllers had obtained good results, they still presented certain issues in practical use. The PD-based robust controllers in [9], [10] faced difficulties when dealing with highly nonlinear systems and also had challenges in parameter adjustment. The design of the improved ADRC in [11] was based on many assumptions, and the parameter adjustment was relatively complex. The adaptive control method [12] required much prior system knowledge, had parameter convergence issues, weak robustness and anti-interference, and high computational complexity that affected real-time performance. The fuzzy controller in [13] could

This work was supported in part by the Postdoctoral Fellowship Program of CPSF under Grant GZC20250940; in part by the project Romanian Hub forArtificial Intelligence-HRIA, Smart Growth, Digitization and Financial Instruments Program, MySMIS under Grant 334906; and in part by the Romanian Ministry of Research, Innovation and Digitization, CNCS/CCCDI-UEFISCDI, within PNCDI IV under Project ERANET-ENUAC-e-MATS. (Corresponding author: Yu Xia.)

Xiao Lin is with the State Key Laboratory of Mechanical Transmission for Advanced Equipment, Chongqing University, Chongqing 400044, China (e-mail: 20210701038@cqu.edu.cn).

Yu Xia is with the State Key Laboratory of Mechanical System and Vibration, School of Mechanical Engineering, Shanghai Jiao Tong University, Shanghai 200240, China (e-mails: rainyx@sjtu.edu.cn).

Zsófia Lendek is with the Department of Automation, Technical University of Cluj-Napoca; Memorandumului 28, 400114, Cluj-Napoca, Romania (e-mail: zsofia.lendek@aut.utcluj.ro).

Radu-Emil Precup is with the Department of Automation and Applied Informatics, Politehnica University of Timisoara, 300223 Timisoara, Romania, and also with the Center for Fundamental and Advanced Technical Research, Romanian Academy-Timisoara Branch, Bd. Mihai Viteazu 24, 300223 Timisoara, Romania (e-mail: radu.precup@aut.upt.ro).

Imre J. Rudas is with the Research and Innovation Centre, Óbuda University, 1034 Budapest, Hungary (e-mail: rudas@uni-obuda.hu).

Ramesh K. Agarwal is with the Department of Mechanical Engineering, Washington University in St. Louis Campus, St. Louis, MO 63130 USA (e-mail: agarwalr@seas.wustl.edu).

effectively deal with uncertainties and nonlinearities during the dynamic process, but its accuracy was relatively low under steady-state conditions. The controller based on SMC in [14], [15] exhibited chattering. Although [16], [17], and [18] were able to mitigate the chattering issue of SMC to some extent, they still faced challenges such as rule design relying on expert experience and limited dynamic learning capability. It can be seen that the control design problem for RJCHRM is very challenging.

Among existing control algorithms, SMC has received widespread attention. However, a significant drawback of SMC is the chattering phenomenon. Super-Twisting SMC (STSMC) can suppress chattering by making the control law continuous through hiding the discontinuous term in the first derivative, and it is easier to design and implement compared with higher order SMC [19]. A novel model-free STSMC strategy for permanent magnet synchronous motor (PMSM) was presented in [20]. [21] proposed an adaptive neural network-based backstepping STSMC framework that achieves high-precision trajectory tracking for underwater manipulators. To enhance current tracking accuracy in active power filter, [22] proposes an adaptive STSMC based on a type-2 fuzzy hybrid neural network. However, there is very little research on SMC, particularly on STSMC in the RJCHRM field. It is of significant academic research value to design STSMC controllers for the RJCHRM, where the current of the PMSM is utilized as the control input, and the output angle or torque of the harmonic reducer is regarded as the output.

For practical engineering applications, attaining an accurate physical system model is problematic. This poses particular challenges to the design of SMC. Over recent years, the excellent approximation features of feed-forward neural networks, such as Radial Basis Function (RBF) neural networks, have made them a hot research topic [23]. An adaptive RBF observer was devised to mitigate the vibration of the aeroelastic system in [24]. In [25], to handle the trajectory tracking issue of uncertain nonlinear systems, a nonlinear controller was proposed by integrating SMC and RBF neural networks. [26] used RBF neural networks to enhance position and force tracking accuracy in cooperative robotic manipulators. Although RBF has achieved good approximation results in these studies, it also has several drawbacks such as poor dynamic characteristics, lack of memory, and limited ability to represent complex structures [27]. The Recurrent Neural Network (RNN) fuses the merits of feed-forward networks with those of feedback networks. [28] proposed an adaptive SMC scheme using a three-layer RNN for nonlinear systems. [29] devised a completely regulated neural network featuring a RNN with two hidden layers and proposed an adaptive global SMC. [30] combined SMC with RNN and proposed an adaptive integral SMC strategy for quadrotor control.

The fuzzy neural network (FNN) [31], [32] combines the knowledge representation ability of the fuzzy logic system [33] and the strong self-learning skill of the neural network. [34] developed an adaptive fuzzy random vector function link-based SMC for robust trajectory tracking of n-link manipulators. An adaptive FNN control using nonsingular terminal SMC for active power filters to achieve finite-time convergence was introduced in [35]. Fusing FNN with RNN can significantly enhance the learning capabilities of complex dynamic systems [36]. [37] proposed an impedance controller based on the recurrent fuzzy wavelet neural network for robotic manipulators. [38] presented a fuzzy double hidden layer RNN control to achieve robust performance for nonlinear systems. To further improve neural network learning performance, [39] designed a type-2 fuzzy recurrent feature selection fuzzy neural network by combining type-2 FNN with RNN. Inspired by the aforementioned research, an adaptive terminal super-twisting controller (ATSC) based on a type-2 fuzzy single hidden layer recurrent neural network (T2FSHLRNN) for RJCHRM is proposed in this research. Compared with existing studies, the main contributions of this research are

1) A modified non-singular terminal sliding surface is proposed. In contrast to the conventional non-singular terminal sliding surface [40], the proposed sliding surface converges faster.
2) A T2FSHLRNN is introduced, which not only takes into account the fuzzy inference ability of the T2FNN, but also incorporates the feature extraction ability of the hidden layer network. A double-layer (internal and external) feedback mechanism is designed. This design allows the network to take into account both the current and previous error information during the approximation process, thus enhancing the approximation accuracy. In addition, the center and base width coefficients can be adjusted adaptively to achieve optimality. In comparison to [41], the novel neural network exhibits enhanced approximation capabilities.
3) For the control of RJCHRM, an adaptive gain function and an ATSC based on T2FSHLRNN are proposed. The adaptability is manifested in two aspects. First, the proposed neural network is combined with the STSMC and parameter learning algorithms are designed, allowing the neural network to adaptively approximate the system uncertainties. Second, variable gains of the STSMC are designed, enabling the system to maintain stability even in the presence of unknown disturbances.
4) The system's stability is proven by Lyapunov synthesis. Furthermore, three simulation experiments are designed to verify the proposed controller. The experimental findings indicate that compared with [15], [41], the steady-state and transient performance are significantly improved.

II. Problem Description

A. Robots joint model composed of harmonic reducer and motor

A typical RJCHRM system is shown in Fig. 1. It consists of a PMSM, a harmonic reducer, and a load. In order to attain high-precision control, these components are treated holistically. The Lagrange energy method [15] is adopted to model the RJCHRM. All notations are specified in Table 1.

The energy composition of the RJCHRM includes both kinetic and potential components. The kinetic portion arises from the motor rotor and load motion, whereas the potential

TABLE I
KEY SYMBOLS USED IN MODELING

Symbol	Description	Unit	Symbol	Description	Unit
P	Elastic potential energy	J	f_s	Friction coefficient	–
K_l	Kinetic energy (Load side)	J	f_1	Friction coefficient	–
F_l	Power loss (Load side)	J	f_2	Friction coefficient	–
K_m	Kinetic energy (Motor side)	J	μ_f	Friction coefficient	–
F_m	Power loss (Motor side)	J	a_0	Taylor expansion coefficient	–
J_m	Moment of inertia of the motor rotor	$kg \cdot m^2$	a_1	Taylor expansion coefficient	–
J_l	Moment of inertia of the load	$kg \cdot m^2$	a_2	Taylor expansion coefficient	–
θ_m	Angular displacement (Motor side)	rad	a_3	Taylor expansion coefficient	–
θ_l	Angular displacement (Load side)	rad	i_d	d-axis current	A
τ	Electromagnetic torque of the motor	$N \cdot m$	i_q	q-axis current	A
B_m	Viscous coefficient of the motor	$N \cdot m \cdot s/rad$	u_q	q-axis voltage	V
τ_{fm}	Friction torque of the harmonic reducer (Motor side)	$N \cdot m$	L	Stator inductance	H
τ_{km}	Elastic deformation torque (Motor side)	$N \cdot m$	n_p	Number of poles	–
N	Transmission ratio	–	R	Stator resistance	Ω
τ_{fl}	Friction torque of the harmonic reducer (Load side)	$N \cdot m$	K	Torque constant of motor	Nm/A
τ_{kl}	Elastic deformation torque (Load side)	$N \cdot m$	$I_{\max}$	Max continuous current	A
f_v	Friction coefficient	–	ψ_f	Rotor flux	Wb
f_c	Friction coefficient	–	θ_d	Desired angular position	rad

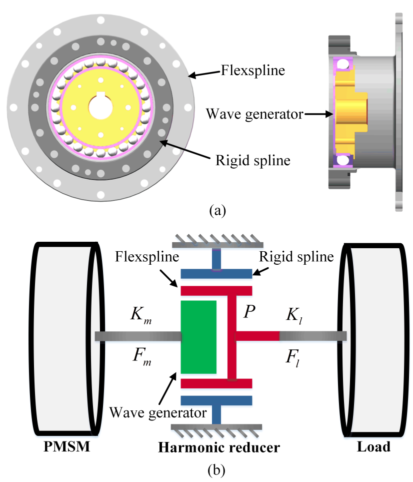

Fig. 1. (a) Structure of harmonic reducer; (b) Energy distribution model of RJCHRM.

energy primarily stems from the harmonic reducer's elastic deformation. The total kinetic energy of the system satisfies

$$K = K_m + K_l = \frac{1}{2}J_m\dot{\theta}_m^2 + \frac{1}{2}J_l\dot{\theta}_l^2. \tag{1}$$

Let $L = K - P$ and $Q = \tau - B_m\dot{\theta}_m - \tau_{fm}$, then the dynamic model of RJCHRM is

$$\frac{d}{dt}\left(\frac{\partial L}{\partial \dot{\theta}_m}\right) - \frac{\partial L}{\partial \theta_m} = Q. \tag{2}$$

Combining (1) with (2) leads to

$$\frac{d}{dt}\left(\frac{\partial K}{\partial \dot{\theta}_m}\right) - \frac{\partial K}{\partial \theta_m} + \frac{\partial P}{\partial \theta_m} = \tau - B_m\dot{\theta}_m - \tau_{fm}, \tag{3}$$

where P is a function of θ_m, and $\partial P/\partial\theta_m = \tau_{km}$ [15] . Introducing $\theta_m = \theta_l N$ into (3) one obtains

$$\frac{J_l\ddot{\theta}_l}{N} + J_m\ddot{\theta}_m + B_m\dot{\theta}_m + \frac{\tau_{fl}}{N} + \frac{\tau_{kl}}{N} = \tau.$$

Here, we use a Stribeck model to calculate τ_{fl} and a third-order Taylor expansion to calculate τ_{kl} . The Stribeck model [9] is

$$\begin{aligned}
\tau_{fl} &= f_v\dot{\theta}_l + f_{n1} + f_{n2},\\
f_{n1} &= f_c sgn\left(\dot{\theta}_l\right)\left(1 - \exp\left(-f_1 \mathrm{sgn}\left(\dot{\theta}_l\right)\dot{\theta}_l\right)^{\mu_f}\right),\\
f_{n2} &= f_s sgn\left(\dot{\theta}_l\right)\exp\left(-f_2 \mathrm{sgn}\left(\dot{\theta}_l\right)\dot{\theta}_l\right)^{\mu_f}.
\end{aligned}$$

The third-order Taylor expansion for calculating τ_{kl} is

$$\begin{aligned}
\tau_{kl} &= a_0 + a_1\Delta\theta + a_2\Delta\theta^2 + a_3\Delta\theta^3,\\
\Delta\theta &= \theta_m/N - \theta_l.
\end{aligned}$$

For PMSM, vector-oriented control stands out as the predominantly utilized control approach. The zero d-axis current control is one of the most typical approaches [9], which achieves the desired torque solely through q-axis current regulation. The mathematical model of a PMSM in the d-q reference frame is

$$\dot{i}_d = 0,$$

$$\dot{i}_q = -\frac{R}{L}i_q - n_p\dot{\theta}_m\frac{\psi_f}{L} + \frac{u_q}{L},$$

$$\tau = \frac{3}{2}n_p\psi_f i_q.$$

Let $x_1 = \theta_l$ and $x_2 = \dot{\theta}_l$ be the state variables, and $u = i_q$ be the system input. Then, the RJCHRM's model is obtained as

$$\begin{cases} \dot{x}_1 = x_2, \\ \dot{x}_2 = f + bu + g, \end{cases} \tag{4}$$

where $f = ax_2$, $a = -\frac{NB_m + f_v/N}{J_l/N + J_mN}$, $b = \frac{3}{2}\frac{n_p\psi_f}{J_l/N + J_mN}$, and $g = -\frac{f_{n1}+f_{n2}+\tau_{kl}}{J_l + J_mN^2}$.

B. Proposed sliding surface

Building upon the traditional non-singular sliding surface, a modified fast non-singular terminal sliding surface (MFNTSS) is introduced:

$$s = \dot{e} + \xi_1 |e|^m sgn\left(e\right) + \xi_2 \delta\left(e\right), \tag{5}$$

where $\xi_1 > 0$, $\xi_2 > 0$, $m > 1$, $n = p/q$, $0 < p < q < 2p$. p and q are odd numbers. The tracking error e is

$$e = \theta_d - \theta_l,$$

where θ_d represents the desired angular position. $\delta\left(e\right)$ in (5) is designed as

$$\delta\left(e\right) = \begin{cases} e^n, |e| \geq \Delta_s, \\ \omega_1 e + \omega_2 e^2, |e| < \Delta_s, \end{cases} \tag{6}$$

where Δ_s represents a very small positive number. ω_1 and ω_2 are designed as

$$\omega_1 = \left(2 - n\right) \Delta_s^{n-1}, \ \omega_2 = \left(-1 + n\right) \Delta_s^{n-2}. \tag{7}$$

The derivative of $\delta\left(e\right)$ is

$$\dot{\delta}\left(e\right) = \begin{cases} n e^{n-1} \dot{e}, |e| \geq \Delta_s, \\ \omega_1 \dot{e} + 2\omega_2 e\dot{e}, |e| < \Delta_s. \end{cases} \tag{8}$$

The analysis of (5) through (8) demonstrates that the proposed sliding surface is differentiable everywhere, and its derivative is also continuous. To illustrate the advantages of MFNTSS, Fig. 2 compares MFNTSS and the traditional non-singular terminal sliding surface [40]. The parameters are chosen as: $\xi_1 = 2$, $\xi_2 = 2$, $m = 3$, $p = 3$, $q = 5$, $\Delta_s = 0.01$. The convergence speed of the MFNTSS surpasses that of the conventional sliding surface by a notable margin.

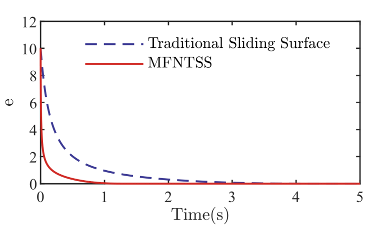

Fig. 2. Comparation between MFNTSS and traditional sliding surface [40].

Remark 1: The advantages of MFNTSS are:

1) Superior convergence: Thanks to the design of the exponential term $\xi_1 |e|^m \mathrm{sgn}\left(\mathrm{e}\right)$, the system will have a faster convergence rate when it is far from the equilibrium state.
2) Non-singular: There are no negative exponent terms when $|e| < \Delta_s$ in (5).
3) Practicality: The term $\dot{e}$ in (5) and (8) does not contain an exponential, making it easier to combine MFNTSS with complex algorithms.

C. Ideal super-twisting controller

The SMC law can be divided into the equivalent control law and the switching control law. To derive the equivalent control law, the derivative of (5) is calculated as

$$\dot{s} = \ddot{e} + \xi_1 m |e|^{m-1} \dot{e} + \xi_2 \dot{\delta}\left(e\right). \tag{9}$$

Substituting (4) into (9) yields

$$\begin{aligned} \dot{s} &= \ddot{e} + \xi_1 m |e|^{m-1} \dot{e} + \xi_2 \dot{\delta}\left(e\right) \\ &= \left(\ddot{\theta}_d - bu - f - g\right) + \xi_1 m |e|^{m-1} \dot{e} + \xi_2 \dot{\delta}\left(e\right). \end{aligned}$$

Let $\dot{s} = 0$, the equivalent control law can be deduced:

$$u_{eq} = \frac{1}{b}\left(\xi_1 m |e|^{m-1} \dot{e} + \xi_1 \dot{\delta}\left(e\right) + \ddot{\theta}_d - \left(f + g\right)\right). \tag{10}$$

The switching control law of STSMC is [41]

$$\begin{cases} u_{sw} = -v/b \\ v = -\zeta_1 |s|^{\frac{1}{2}} \mathrm{sgn}\left(s\right) + w \\ \dot{w} = -\zeta_2 \mathrm{sgn}\left(s\right) \end{cases}, \tag{11}$$

where v is a robustness term, $\zeta_1 > 0$, $\zeta_2 > 0$ are the fixed gains.

By combining (10) and (11), the ideal STSMC law can be obtained as

$$\begin{aligned} u &= u_{eq} + u_{sw} \\ &= \tfrac{1}{b}\left(\xi_1 m |e|^{m-1} \dot{e} + \xi_1 \dot{\delta}\left(e\right) + \ddot{\theta}_d - \left(f + g\right)\right) + \tfrac{1}{b}\left(-v\right). \end{aligned}$$

A rational choice of values for ζ_1 and ζ_2 can ensures system stability [41].

III. The Proposed Neural Network

In practical control systems, there are various uncertainties. For example, system parameters may change due to factors such as environmental variations and equipment aging. This parametric uncertainty can affect the performance of the system. A new type of neural network is proposed in this section for the online approximation of uncertainty modeling of RJCHRM.

A. Structure of T2FSHLRNN

The T2FSHLRNN (Fig. 3) is a network featuring two feedback loops. Within its external and internal feedback loops, the output signal from the preceding step is fed back to the respective layer. The network consists of eight layers, namely the input layer, the membership layer, the rule layer, a second input layer, the hidden layer, the fusion layer, the type-reduction layer and the output layer. The basic functions of each layer are introduced as follows.

Layer 1-the first input layer: The primary role of this layer is to receive the incoming signal. $X^1 = \left[x_1^1, x_2^1, \ldots x_m^1\right]^T \in R^{m \times 1}$ and the output signal exY from the eighth layer. The connection weight between the output layer and this layer is $W_O = \left[w_{O1}, w_{O2}, \ldots, w_{Om}\right]^T \in R^{m \times 1}$. The output of the i-th node is given by:

$$y_i^1 = x_i \cdot exY \cdot W_{Oi} \ \left(i = 1, 2, \ldots, m\right),$$

with the output of the layer being

$$Y^1 = \left[y_1^1, y_2^1, \dots y_m^1\right]^T \in R^{m\times 1}.$$

Layer 2-the membership layer: Each output from the first layer is interfaced with two neurons within this layer. The neurons execute a fuzzification operation on the input signals by means of the type-2 fuzzy membership function, thereby augmenting the neural network's capacity to cope with non-linearities.

The membership degree is calculated using the Gaussian function [39]. Define the lower and upper limits of fuzzification as

$$\underline{\mu}_j^i = \exp\left(-\frac{\left(x_{ij}^2 - q_j^i\right)^2}{\left(\underline{p}_j^i\right)^2}\right), \overline{\mu}_j^i = \exp\left(-\frac{\left(x_{ij}^2 - q_j^i\right)^2}{\left(\overline{p}_j^i\right)^2}\right),$$

where $x_{ij}^2 = y_i^1$ is the input to node j of this layer, q_j^i is the center, and $\overline{p}_j^i$ and $\underline{p}_j^i$ are the upper and lower base widths of the type-2 Gaussian membership function. Each node's output is

$$y_{ij}^2 = \left[\mu_j^i\right] = \left[\underline{\mu}_j^i, \overline{\mu}_j^i\right] \quad (i = 1, 2, \dots m; j = 1, 2, \dots, n).$$

Define the center vector as

$$\begin{aligned} Q = [&q_1^1, q_2^1, \dots, q_n^1, q_1^2, q_2^2, \\ &\dots, q_n^2, q_1^m, q_2^m, \dots, q_n^m] \in R^{mn\times 1}, \end{aligned}$$

and the upper and lower base width vectors as

$$\begin{aligned} \overline{P} = [&\overline{p}_1^1, \overline{p}_2^1, \dots, \overline{p}_n^1, \overline{p}_1^2, \overline{p}_2^2, \\ &\dots, \overline{p}_n^2, \overline{p}_1^m, \overline{p}_2^m, \dots, \overline{p}_n^m] \in R^{mn\times 1}, \end{aligned}$$

$$\begin{aligned} \underline{P} = \Big[&\underline{p}_1^1, \underline{p}_2^1, \dots, \underline{p}_n^1, \underline{p}_1^2, \underline{p}_2^2, \\ &\dots, \underline{p}_n^2, \underline{p}_1^m, \underline{p}_2^m, \dots, \underline{p}_n^m\Big] \in R^{mn\times 1}. \end{aligned}$$

The output vector of the membership layer is

$$\begin{aligned} Y^2 = &\left[y_{11}^2, y_{12}^2, \dots y_{1n}^2,\ \ y_{21}^2, y_{22}^2,\right. \\ &\left.\dots y_{2n}^2, \dots, y_{m1}^2, y_{m2}^2, \dots y_{mn}^2\right]^T \\ = &\left[\mu_1^1, \mu_2^1, \dots \mu_n^1,\ \ \mu_1^2, \mu_2^2,\right. \\ &\left.\dots \mu_n^2, \dots, \mu_1^m, \mu_2^m, \dots \mu_n^m\right]^T \in R^{2mn\times 1}. \end{aligned}$$

Layer 3-the rule layer: integrates the output data of the second layer. This layer computes

$$F_j = \left[\underline{f}_j, \overline{f}_j\right]^T = \left[\underline{\mu}_j^1 \cdot \underline{\mu}_j^2 \cdot \dots \cdot \underline{\mu}_j^m,\ \overline{\mu}_j^1 \cdot \overline{\mu}_j^2 \cdot \dots \cdot \overline{\mu}_j^m\right]^T.$$

The values are normalized

$$F_{Nj} = \left[\underline{f}_{Nj}, \overline{f}_{Nj}\right]^T = \left[\frac{\underline{f}_j}{\sum\limits_{j=1}^{n} \underline{f}_j}, \frac{\overline{f}_j}{\sum\limits_{j=1}^{n} \overline{f}_j}\right]^T,$$

and the output vector of this layer is obtained as

$$Y^3 = \left[F_{N1}, F_{N2}, \dots, F_{Nn}\right]^T \in R^{n\times 1}.$$

Layer 4-the second input layer: This layer is used to transfer the output of the first layer. , i.e.,

$$Y^4 = \left[y_1^4, y_2^4, \dots y_m^4\right]^T = Y^1 = \left[y_1^1, y_2^1, \dots y_m^1\right]^T \in R^{m\times 1}.$$

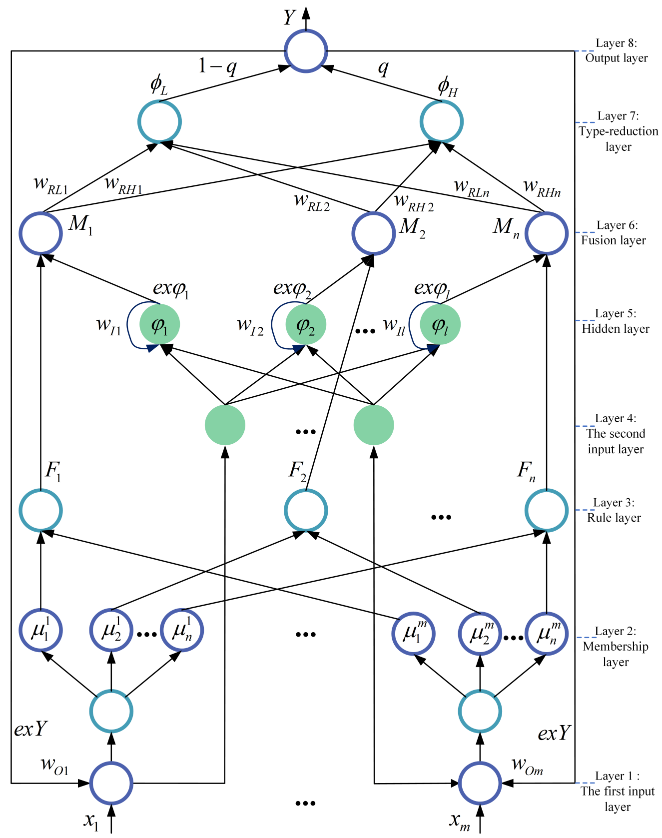

Fig. 3. Structure diagram of T2FSHLRNN.

Layer 5-the hidden layer: extracts input features and improves approximation accuracy. To mitigate the computational complexity, a single hidden layer is used. In addition, a feedback loop is formed within this layer so as to feedback the output of the neurons from the previous operation step. The output of each node is

$$\varphi_k = \exp\left(-\frac{\sum\limits_{i=1}^{m}\left(y_i^4 + w_{Ik}\cdot ex\varphi_k - c_k\right)^2}{b_k^2}\right),$$

resulting in $Y^5 = \left[\varphi_1, \varphi_2, \dots \varphi_m\right]^T \in R^{m\times 1}$, where $k = 1, 2, \dots, n$, c_k is the center vector and b_k is the base width of the Gaussian function, w_{Ik} is the weight of the internal feedback loop, and $ex\varphi_k$ is the output signal of the k-th hidden layer at the previous time instant. The center, the base width and the weight vectors are

$$C = \left[c_1, c_2, \dots, c_n\right] \in R^{n\times 1},$$

$$B = \left[b_1, b_2, \dots, b_n\right] \in R^{n\times 1},$$

$$W_I = \left[w_{I1}, w_{I2}, \dots, w_{In}\right] \in R^{n\times 1}.$$

Layer 6-the fusion layer: integrates the output signals from the third and fifth layers. For the *j*-th node in this layer, fusion yields

$$\begin{aligned} M_j = F_{Nj} \cdot \varphi_j = \left[\underline{f}_{Nj}, \overline{f}_{Nj}\right]^T \cdot \varphi_j \\ = \left[\underline{f}_{Nj} \cdot \varphi_j, \overline{f}_{Nj} \cdot \varphi_j\right]^T = \left[\underline{M}_j, \overline{M}_j\right]^T. \end{aligned}$$

The output of this layer is

$$Y^6 = \left[\underline{M}_1, \overline{M}_1, \underline{M}_2, \overline{M}_2, \ldots \underline{M}_n, \overline{M}_n\right]^T \in R^{2n\times 1}.$$

Layer 7-the type-reduction layer: combines previous information. Its output vector is defined as

$$\begin{aligned} Y^7 &= [\phi_H, \phi_L]^T, \\ \phi_H &= \sum_{j=1}^{n} w_{RHj} \cdot \overline{M}_j = W_{RH}^T \cdot \overline{M}, \\ \phi_L &= \sum_{j=1}^{n} w_{RLj} \cdot \underline{M}_j = W_{RL}^T \cdot \underline{M}, \end{aligned}$$

where ϕ_H and ϕ_L are the upper and lower outputs of this layer, w_{RHj} and w_{RLj} are the upper and lower weights of each node. The expressions for W_{RH}, W_{RL}, $\overline{M}$ and $\underline{M}$ are

$$\begin{aligned} W_{RH} &= [w_{RH1}, w_{RHj}, \ldots, w_{RHn}]^T \in R^{n\times 1}, \\ W_{RL} &= [w_{RL1}, w_{RLj}, \ldots, w_{RLn}]^T \in R^{n\times 1}, \\ \overline{M} &= \left[\overline{M}_1, \overline{M}_2, \ldots, \overline{M}_n\right]^T \in R^{n\times 1}, \\ \underline{M} &= \left[\underline{M}_1, \underline{M}_2, \ldots, \underline{M}_n\right]^T \in R^{n\times 1}. \end{aligned}$$

Layer 8-the output layer: computes the average of the signals from the 7th layer:

$$\begin{aligned} Y^8 &= \tfrac{1}{2}\left(\phi_H + \phi_L\right) = \tfrac{1}{2}\left(W_{RH}^T \cdot \overline{M} + W_{RL}^T \cdot \underline{M}\right) \\ &= \tfrac{1}{2}\begin{pmatrix} W_{RH}^T & W_{RL}^T \end{pmatrix}\begin{pmatrix} \overline{M} \\ \underline{M} \end{pmatrix} = \tfrac{1}{2}W^T M, \end{aligned} \tag{12}$$

where the expressions of W and M are

$$\begin{aligned} W = [&w_{RH1}, w_{RHj}, \ldots, w_{RHn}, \\ &w_{RL1}, w_{RLj}, \ldots, w_{RLn}]^T \in R^{2n\times 1}, \end{aligned}$$

$$M = \left[\overline{M}_1, \overline{M}_2, \ldots, \overline{M}_n, \underline{M}_1, \underline{M}_2, \ldots, \underline{M}_n\right]^T \in R^{2n\times 1}.$$

Remark 2: The proposed network has the following advantages:

1) As can be inferred from the designs of Layer 2 and Layer 7, T2FSHLRNN incorporates T2FNN. In comparison with the RNNs in [28]–[30], it can better handle the uncertainties and ambiguities inherent in data.
2) Thanks to the double-feedback design, T2FSHLRNN integrates RNN. This integration enables the network to take into account both the current and previous error information, thereby enhancing the approximation accuracy.
3) From the perspective of the hidden layer (Layer 5), T2FSHLRNN assimilates the feature-extraction capability of the hidden-layer network.
4) Thanks to the fusion layer (Layer 6), when one neural network in T2FSHLRNN is learning parameters online, it considers the output state of another neural network. This implies that the neural network possesses a more robust global learning ability.
5) Initial values for the base width and center vector of T2FSHLRNN can be specified without any constraints. Furthermore, its parameters can be adaptively tuned, see Section III B, to attain optimal values. In comparison to the neural network characterized by fixed base width and center vector [27], [41], T2FSHLRNN offers greater convenience in application.

All these characteristics contribute to a higher approximation accuracy of T2FSHLRNN.

B. Parameter learning algorithm

The T2FSHLRNN is used to online approximate f in (4) in this research. In order to attain this objective, the sliding surface s is employed as the input signal for the neural network, with (12) being the approximation value.

Assumption 1: There exist optimal parameters such that

$$f = \frac{1}{2}W^{*T}M^*\left(s, W_O^*, Q^*, \overline{P}^*, \underline{P}^*, C^*, B^*, W_I^*\right) + \varepsilon,$$

where W^*, W_O^*, Q^*, $\overline{P}^*$, $\underline{P}^*$, C^*, B^* and W_I^* are the optimal parameters. ε is the minimum approximation error.

The output of T2FSHLRNN is

$$\hat{f} = \frac{1}{2}\hat{W}^T\hat{M}\left(s, \hat{W}_O, \hat{Q}, \hat{\overline{P}}, \underline{\hat{P}}, \hat{C}, \hat{B}, \hat{W}_I\right),$$

where $\hat{W}$, $\hat{W}_O$, $\hat{Q}$, $\hat{\overline{P}}$, $\underline{\hat{P}}$, $\hat{C}$, $\hat{B}$, $\hat{W}_I$ are the estimated parameters.

The discrepancy between the approximated value and the ideal value is

$$\begin{aligned} \hat{f} - f &= \tfrac{1}{2}\hat{W}^T\hat{M} - \tfrac{1}{2}W^{*T}M^* - \varepsilon \\ &= -\tfrac{1}{2}W^{*T}\left(\hat{M} + \tilde{M}\right) + \tfrac{1}{2}\hat{W}^T\hat{M} - \varepsilon \\ &= -\tfrac{1}{2}\tilde{W}^T\hat{M} - \tfrac{1}{2}\hat{W}^T\tilde{M} - \tfrac{1}{2}\tilde{W}^T\tilde{M} - \varepsilon \\ &= -\tfrac{1}{2}\tilde{W}^T\hat{M} - \tfrac{1}{2}\hat{W}^T\tilde{M} - \varepsilon_0, \end{aligned} \tag{13}$$

where $\tilde{W} = W^* - \hat{W}$ and $\varepsilon_0 = \frac{1}{2}\tilde{W}^T\tilde{M} + \varepsilon$. To derive the parameter learning law of the T2FSHLRNN, the Taylor expansion of M^* is carried out

$$\begin{aligned} &M^*\left(Q^*, W_O^*, \overline{P}^*, \underline{P}^*, C^*, B^*, W_I^*\right) \\ &= \hat{M}\left(\hat{Q}, \hat{W}_O, \hat{\overline{P}}, \underline{\hat{P}}, \hat{C}, \hat{B}, \hat{W}_I\right) \\ &\quad + O_s + \left.\tfrac{\partial M}{\partial W_O^*}\right|_{W_I^* = \hat{W}_I}\left(W_O^* - \hat{W}_O\right) \\ &\quad + \left.\tfrac{\partial M}{\partial Q^*}\right|_{Q^* = \hat{Q}}\left(Q^* - \hat{Q}\right) + \left.\tfrac{\partial M}{\partial \overline{P}^*}\right|_{\overline{P}^* = \hat{\overline{P}}}\left(\overline{P}^* - \hat{\overline{P}}\right) \\ &\quad + \left.\tfrac{\partial M}{\partial \underline{P}^*}\right|_{\underline{P}^* = \underline{\hat{P}}}\left(\underline{P}^* - \underline{\hat{P}}\right) + \left.\tfrac{\partial M}{\partial C^*}\right|_{C^* = \hat{C}}\left(C^* - \hat{C}\right) \\ &\quad + \left.\tfrac{\partial M}{\partial B^*}\right|_{B^* = \hat{B}}\left(B^* - \hat{B}\right) + \left.\tfrac{\partial M}{\partial W_I^*}\right|_{W_I^* = \hat{W}_I}\left(W_I^* - \hat{W}_I\right). \end{aligned}$$

The difference between the approximated value $\hat{M}$ and the ideal value M^* is

$$\begin{aligned}
&\tilde{M}\left(\tilde{Q},\tilde{W}_O,\tilde{\overline{P}},\underline{\tilde{P}},\tilde{C},\tilde{B},\tilde{W}_I\right) = M^* - \hat{M} \\
&= \left.\frac{\partial M}{\partial W_O^*}\right|_{W_O^*=\hat{W}_O}\left(W_O^*-\hat{W}_O\right) + \left.\frac{\partial M}{\partial Q^*}\right|_{Q^*=\hat{Q}}\left(Q^*-\hat{Q}\right) \\
&\quad + \left.\frac{\partial M}{\partial \overline{P}^*}\right|_{\overline{P}^*=\hat{\overline{P}}}\left(\overline{P}^*-\hat{\overline{P}}\right) + \left.\frac{\partial M}{\partial \underline{P}^*}\right|_{\underline{P}^*=\hat{\underline{P}}}\left(\underline{P}^*-\hat{\underline{P}}\right) \\
&\quad + \left.\frac{\partial M}{\partial C^*}\right|_{C^*=\hat{C}}\left(C^*-\hat{C}\right) + \left.\frac{\partial M}{\partial B^*}\right|_{B^*=\hat{B}}\left(B^*-\hat{B}\right) \\
&\quad + \left.\frac{\partial M}{\partial W_I^*}\right|_{W_I^*=\hat{W}_I}\left(W_I^*-\hat{W}_I\right) + O_s \\
&= M_{W_O}\cdot\tilde{W}_O + M_Q\cdot\tilde{Q} + M_{\overline{P}}\cdot\tilde{\overline{P}} + M_{\underline{P}}\cdot\tilde{\underline{P}} \\
&\quad + M_C\cdot\tilde{C} + M_B\cdot\tilde{B} + M_{W_I}\cdot\tilde{W}_I + O_s,
\end{aligned} \tag{14}$$

where M_{W_O}, M_Q, $M_{\overline{P}}$, $M_{\underline{P}}$, M_C, M_B, M_{W_I} are the derivative of M wrt. W_O^*, Q^*, $\overline{P}^*$, $\underline{P}^*$, C^*, B^* and W_I^*. O_s represents the high order terms. M_{W_O}, M_Q, $M_{\overline{P}}$, $M_{\underline{P}}$, M_C, M_B and M_{W_I} are the partial derivatives of M with respect to each variable evaluated at their approximate values. As a representative example, M_{W_O} is given by:

$$\begin{aligned}
M_{W_O} &= \left.\frac{\partial M}{\partial W_O{}^*}\right|_{W_O{}^*=\hat{W}_O} \\
&= \begin{bmatrix} \frac{\partial \overline{M}_1}{\partial W_O} & \frac{\partial \overline{M}_2}{\partial W_O} & \cdots & \frac{\partial \underline{M}_n}{\partial W_O} \end{bmatrix}^T_{2n\times m}.
\end{aligned}$$

Substituting (14) into (13) yields

$$\begin{aligned}
&\hat{f}-f = -\tfrac{1}{2}\tilde{W}^T\hat{M} - \tfrac{1}{2}\hat{W}^T\tilde{M} - \varepsilon_0 \\
&= -\tfrac{1}{2}\tilde{W}^T\hat{M} - \tfrac{1}{2}\hat{W}^T\Big(M_{W_O}\cdot\tilde{W}_O + M_Q\cdot\tilde{Q} + M_{\overline{P}}\cdot\tilde{\overline{P}} \\
&\quad + M\cdot\tilde{\underline{P}} + M_C\cdot\tilde{C} + M_B\cdot\tilde{B} + M_{W_I}\cdot\tilde{W}_I + O_s\Big) - \varepsilon_0 \\
&= -\tfrac{1}{2}\tilde{W}^T\hat{M} - \tfrac{1}{2}\hat{W}^T M_{W_O}\cdot\tilde{W}_O - \tfrac{1}{2}\hat{W}^T M_Q\cdot\tilde{Q} \\
&\quad - \tfrac{1}{2}\hat{W}^T M_{\overline{P}}\cdot\tilde{\overline{P}} - \tfrac{1}{2}\hat{W}^T M_{\underline{P}}\cdot\tilde{\underline{P}} - \tfrac{1}{2}\hat{W}^T M_C\cdot\tilde{C} \\
&\quad - \tfrac{1}{2}\hat{W}^T M_B\cdot\tilde{B} - \tfrac{1}{2}\hat{W}^T M_{W_I}\cdot\tilde{W}_I - O_m,
\end{aligned} \tag{15}$$

where $O_m = \frac{1}{2}\hat{W}^T O_s + \varepsilon_0$.

The following parameter learning algorithms are designed:

$$\dot{\hat{W}} = \dot{\tilde{W}} = \frac{\varpi_1}{2}s\hat{M}, \tag{16}$$

$$\dot{\hat{W}}_O^T = \dot{\tilde{W}}_O^T = \frac{\varpi_2}{2}s\hat{W}^T M_{W_O}, \tag{17}$$

$$\dot{\hat{Q}}^T = \dot{\tilde{Q}}^T = \frac{\varpi_3}{2}s\hat{W}^T M_Q, \tag{18}$$

$$\dot{\hat{\overline{P}}}^T = \dot{\tilde{\overline{P}}}^T = \frac{\varpi_4}{2}s\hat{W}^T M_{\overline{P}}, \tag{19}$$

$$\dot{\hat{\underline{P}}}^T = \dot{\tilde{\underline{P}}}^T = \frac{\varpi_5}{2}s\hat{W}^T M_{\underline{P}}, \tag{20}$$

$$\dot{\hat{C}}^T = \dot{\tilde{C}}^T = \frac{\varpi_6}{2}s\hat{W}^T M_C, \tag{21}$$

$$\dot{\hat{B}}^T = \dot{\tilde{B}}^T = \frac{\varpi_7}{2}s\hat{W}^T M_B, \tag{22}$$

$$\dot{\hat{W}}_I{}^T = \dot{\tilde{W}}_I{}^T = \frac{\varpi_8}{2}s\hat{W}^T M_{W_I}, \tag{23}$$

where ϖ_1, ϖ_2, ϖ_3, ϖ_4, ϖ_5, ϖ_6, ϖ_7, ϖ_8 are learning rates.

IV. ATSC Based on T2FSHLRNN

In practical control systems, the system is often influenced by disturbances. Experimental determination of the supremum values for both the disturbance term and its temporal derivative poses significant practical challenges in physical implementations. If the coefficients of the super twisting control are fixed like in [21], then when facing disturbances, the control system may not be able to compensate effectively. Variable gains for super-twisting control are proposed to handle the uncertain disturbances in this section.

A. Design of ATSC based on T2FSHLRNN

Compared with the ideal STSMC law in Section II.C, a novel robust term is designed as (24), while the other parts remain unchanged.

$$\begin{cases} v = -\chi_1\left(|s|^{\frac{1}{2}}\operatorname{sgn}(s) + \chi_3|s|^{\varphi}sgn(s)\right) + w \\ \dot{w} = -\chi_2\left(\frac{1}{2} + \chi_3\left(\varphi+\frac{1}{2}\right)|s|^{\varphi-1/2} + \chi_3^2\varphi|s|^{2\varphi-1}\right)sgn(s). \end{cases} \tag{24}$$

In (24), χ_1, χ_2 are adaptive gains, $\chi_2 > 0$, $\varphi > 1$. This research proposes the following adaptive gain function

$$\begin{aligned}
\dot{\chi}_1 &= \begin{cases} \pi_1\sqrt{\frac{\gamma_1}{2}}\tanh\kappa\left(|s|-\mu\right), \chi_1 > \chi_\Delta \\ \rho, \chi_1 \le \chi_\Delta, \end{cases} \\
\chi_2 &= \sigma\chi_1 + \tfrac{1}{2}\left(\lambda + 4\sigma^2\right),
\end{aligned} \tag{25}$$

$$\rho = \pi_1\sqrt{\gamma_1/2}, \tag{26}$$

$$\sigma = \frac{\pi_2}{\pi_1}\sqrt{\frac{\gamma_2}{\gamma_1}}, \tag{27}$$

where π_1, γ_1, μ, λ, χ_Δ, κ, π_2, γ_2 are positive constants that need to be designed, and $\chi_1(0) > \chi_\Delta$.

Assumption 2: The disturbance and its derivative are bounded as:

$$|d| \le M_D, \left|\dot{d}\right| \le M_d,$$

where M_D and M_d are unknown positive constants.

Remark 3: Rationality analysis of Assumption 2.

1) In practical scenarios, disturbances that impact actual systems generally possess finite energy and a restricted rate of change. Consequently, Assumption 2 has become a prevalent postulate within the domain of disturbance rejection control, as seen in [42]. Its efficacy has been corroborated through multiple successful controller design implementations, see e.g., [24], [42], [43].
2) Under the STSMC framework established in [42], the system boundaries must be presumed identifiable. However, precise numerical values delineating the boundaries of the disturbance and its derivative are not needed in Assumption 2. Merely establishing the existence of such boundaries suffices. When contrasted with the approach in [42], Assumption 2 herein is more accommodating.

Remark 4: Advantages of the proposed robust term.

1) The proposed robust term and parameter selection does not require prior knowledge of disturbance bounds or their derivatives, fundamentally avoiding the gain-overestimation problem compared with [42];

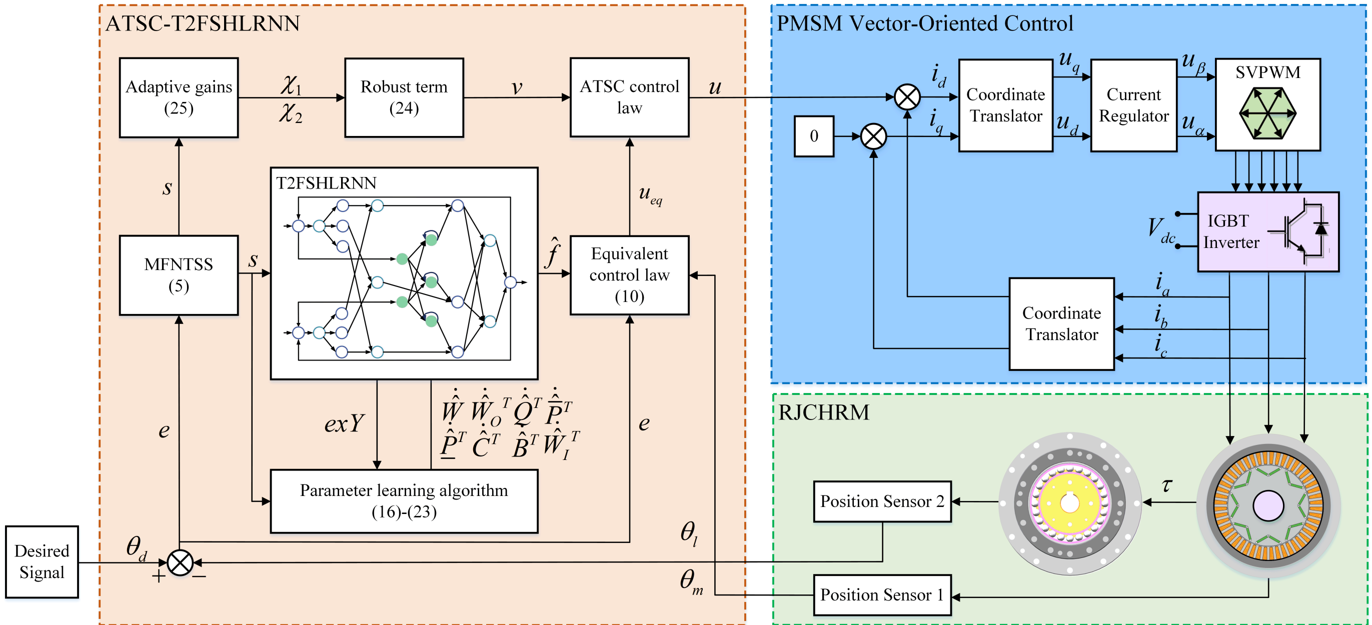

Fig. 4. Control scheme of RJCHRM.

2) Through the introduced feedback term $\chi_3|s|^{\varphi} sgn\left(s\right)$ in robust term, the designed ATSC can exhibit superior convergence speed versus [41] even when system states remain distant from the sliding surface.

Fig. 4 depicts the control scheme of RJCHRM. RJCHRM transmits the angle and angular velocity in real-time to ATSC-T2FSHLRNN. ATSC-T2FSHLRNN calculates the ideal required current. Then, PMSM Vector-Oriented Control modulates the actual control current for the PMSM, thus closing the loop.

B. Stability analysis

In order to demonstrate the system's stability, the following Lyapunov function is selected:

$$V = V_1 + V_2,$$

where

$$V_1 = V_0 + \frac{1}{2\gamma_1}(\chi_1 - \chi_1^*)^2 + \frac{1}{2\gamma_2}(\chi_2 - \chi_2^*)^2,$$

$$\begin{aligned}
&V_0 = Z^T P Z,\\
&Z = \begin{bmatrix} |s|^{\frac{1}{2}}\mathrm{sgn}\left(s\right) + \chi_3|s|^{\varphi} sgn\left(s\right) \\ w \end{bmatrix} = \begin{bmatrix} \psi\left(s\right) \\ w \end{bmatrix},\\
&P = \begin{bmatrix} p_{11} & p_{12} \\ p_{21} & p_{22} \end{bmatrix} = \begin{bmatrix} \lambda + 4\sigma^2 & -2\sigma \\ -2\sigma & 1 \end{bmatrix},
\end{aligned}$$

$$\begin{aligned}
V_2 = {} & \tfrac{1}{2}s^2 + \tfrac{1}{2\varpi_1}\tilde{W}^T\tilde{W} + \tfrac{1}{2\varpi_2}\tilde{W}_O^T\tilde{W}_O + \tfrac{1}{2\varpi_3}\tilde{Q}^T\tilde{Q}\\
& + \tfrac{1}{2\varpi_4}\tilde{\overline{P}}^T\tilde{\overline{P}} + \tfrac{1}{2\varpi_5}\tilde{\underline{P}}^T\tilde{\underline{P}} + \tfrac{1}{2\varpi_6}\tilde{C}^T\tilde{C}\\
& + \tfrac{1}{2\varpi_7}\tilde{B}^T\tilde{B} + \tfrac{1}{2\varpi_8}\tilde{W}_I^T\tilde{W}_I,
\end{aligned} \tag{28}$$

where γ_1, γ_2, χ_1^*, χ_2^*, λ, σ are positive constants. The derivative of V_1 is

$$\begin{aligned}
\dot{V}_1 &= \dot{V}_0 + \tfrac{1}{\gamma_1}\left(\chi_1 - \chi_1^*\right)\dot{\chi}_1 + \tfrac{1}{\gamma_2}\left(\chi_2 - \chi_2^*\right)\dot{\chi}_2\\
&= \dot{Z}^T P Z + Z^T P \dot{Z} + \tfrac{1}{\gamma_1}\left(\chi_1 - \chi_1^*\right)\dot{\chi}_1 + \tfrac{1}{\gamma_2}\left(\chi_2 - \chi_2^*\right)\dot{\chi}_2\\
&= \dot{\psi}\left(s\right) Z^T\left({Q_V}^T P + P Q_V\right) Z + \tfrac{1}{\gamma_1}\left(\chi_1 - \chi_1^*\right)\dot{\chi}_1 +\\
&\quad \tfrac{1}{\gamma_2}\left(\chi_2 - \chi_2^*\right)\dot{\chi}_2\\
&= \dot{\psi}\left(s\right) Z^T\Theta Z + \tfrac{1}{\gamma_1}\left(\chi_1 - \chi_1^*\right)\dot{\chi}_1 + \tfrac{1}{\gamma_2}\left(\chi_2 - \chi_2^*\right)\dot{\chi}_2,
\end{aligned} \tag{29}$$

where

$$Q_V = \begin{bmatrix} -\chi_1 & 1 \\ -\chi_2 & 0 \end{bmatrix},\ \dot{\psi}\left(s\right) = \frac{1}{2}|s|^{-\frac{1}{2}},$$

$$\begin{aligned}
\Theta &= Q_V^T P + P Q_V\\
&= \begin{bmatrix} -2\chi_1\left(\lambda + 4\sigma^2\right) + 8\chi_2\sigma & 2\chi_1\sigma - 2\chi_2 + \lambda + 4\sigma^2 \\ 2\chi_1\sigma - 2\chi_2 + \lambda + 4\sigma^2 & -4\sigma \end{bmatrix}.
\end{aligned} \tag{30}$$

Substituting χ_2 in (25) into (30), and we get

$$\begin{aligned}
\Theta &= \begin{bmatrix} -2\chi_1\left(\lambda + 4\sigma^2\right) + 8\left(\sigma\chi_1 + \frac{1}{2}\left(\lambda + 4\sigma^2\right)\right)\sigma & 0 \\ 0 & -4\sigma \end{bmatrix}\\
&= \begin{bmatrix} -2\chi_1\lambda + 4\sigma\left(\lambda + 4\sigma^2\right) & 0 \\ 0 & -4\sigma \end{bmatrix}.
\end{aligned} \tag{31}$$

$-2\chi_1\lambda + 4\sigma\left(\lambda + 4\sigma^2\right) < 0$, if

$$\chi_1 > 2\sigma\left(\lambda + 4\sigma^2\right)/\lambda. \tag{32}$$

Moreover, $\dot{V}_0$ satisfies

$$\begin{aligned}
\dot{V}_0 &= \dot{\psi}\left(s\right) Z^T\Theta Z \le \dot{\psi}\left(s\right) p_{\min}\left(\Theta\right)\|Z\|_2^2\\
&\le \tfrac{1}{2}p_{\min}\left(\Theta\right)\|Z\| \le \tfrac{1}{2}p_{\min}\left(\Theta\right)\sqrt{V_0/p_{\max}\left(P\right)}\\
&= rV_0^{1/2} \le 0,
\end{aligned} \tag{33}$$

where $r = 0.5p_{\min}(\Theta)/p_{\max}^{1/2}(P)$, $p_{\min}(\Theta)$ stands for the minimum eigenvalue of Θ in (31), while $p_{\max}(P)$ denotes the maximum eigenvalue of P. Substituting (33) into (29) yields

$$\begin{aligned}\dot{V}_1 &\le rV_0^{1/2} + \tfrac{1}{\gamma_1}(\chi_1-\chi_1^*)\dot{\chi}_1 + \tfrac{1}{\gamma_2}(\chi_2-\chi_2^*)\dot{\chi}_2\\ &\le -\left[r^2V_0 + \tfrac{\pi_1^2}{2\gamma_1}(\chi_1-\chi_1^*)^2 + \tfrac{\pi_2^2}{2\gamma_2}(\chi_2-\chi_2^*)^2\right]^{\frac{1}{2}}\\ &\quad + \tfrac{1}{\gamma_1}(\chi_1-\chi_1^*)\dot{\chi}_1 + \tfrac{1}{\gamma_2}(\chi_2-\chi_2^*)\dot{\chi}_2\\ &\quad + \tfrac{\pi_1}{\sqrt{2\gamma_1}}|\chi_1-\chi_1^*| + \tfrac{\pi_2}{\sqrt{2\gamma_2}}|\chi_2-\chi_2^*|\\ &\le -r_mV_1^{\frac{1}{2}} + \tfrac{1}{\gamma_1}(\chi_1-\chi_1^*)\dot{\chi}_1 + \tfrac{1}{\gamma_2}(\chi_2-\chi_2^*)\dot{\chi}_2\\ &\quad + \tfrac{\pi_1}{\sqrt{2\gamma_1}}|\chi_1-\chi_1^*| + \tfrac{\pi_2}{\sqrt{2\gamma_2}}|\chi_2-\chi_2^*|,\end{aligned} \tag{34}$$

where π_1 and π_2 are positive constants, $\gamma_m = \min(\gamma, \pi_1, \pi_2)$. According to the adaptive gains (25), χ_1 and χ_2 are bounded, and therefore there must exist χ_1^* and χ_2^* such that$\chi_1 - \chi_1^* = \varepsilon_{\chi_1} < 0$ and $\chi_2 - \chi_2^* = \varepsilon_{\chi_2} < 0$ hold true. Then (34) can transform into

$$\begin{aligned}\dot{V}_1 &\le -r_mV_1^{\frac{1}{2}} + \tfrac{1}{\gamma_1}\varepsilon_{\chi_1}\dot{\chi}_1 + \tfrac{1}{\gamma_2}\varepsilon_{\chi_2}\dot{\chi}_2\\ &\quad + \tfrac{\pi_1}{\sqrt{2\gamma_1}}|\varepsilon_{\chi_1}| + \tfrac{\pi_2}{\sqrt{2\gamma_2}}|\varepsilon_{\chi_2}|\\ &= -r_mV_1^{\frac{1}{2}} - \tfrac{1}{\gamma_1}|\varepsilon_{\chi_1}|\dot{\chi}_1 - \tfrac{1}{\gamma_2}|\varepsilon_{\chi_2}|\dot{\chi}_2\\ &\quad + \tfrac{\pi_1}{\sqrt{2\gamma_1}}|\varepsilon_{\chi_1}| + \tfrac{\pi_2}{\sqrt{2\gamma_2}}|\varepsilon_{\chi_2}|\\ &= -r_mV_1^{\frac{1}{2}} - |\varepsilon_{\chi_1}|\left(\tfrac{1}{\gamma_1}\dot{\chi}_1 - \tfrac{\pi_1}{\sqrt{2\gamma_1}}\right)\\ &\quad - |\varepsilon_{\chi_2}|\left(\tfrac{1}{\gamma_2}\dot{\chi}_2 - \tfrac{\pi_2}{\sqrt{2\gamma_2}}\right)\\ &= -r_mV_1^{\frac{1}{2}} + \Psi,\end{aligned} \tag{35}$$

where

$$\Psi = -|\varepsilon_{\chi_1}|\left(\frac{1}{\gamma_1}\dot{\chi}_1 - \frac{\pi_1}{\sqrt{2\gamma_1}}\right) - |\varepsilon_{\chi_2}|\left(\frac{1}{\gamma_2}\dot{\chi}_2 - \frac{\pi_2}{\sqrt{2\gamma_2}}\right). \tag{36}$$

Taking the derivative of (28) yields

$$\begin{aligned}\dot{V}_2 &= s\dot{s} + \tfrac{1}{\varpi_1}\tilde{W}^T\dot{\tilde{W}} + \tfrac{1}{\varpi_2}\tilde{W}_O^T\dot{\tilde{W}}_O + \tfrac{1}{\varpi_3}\tilde{Q}^T\dot{\tilde{Q}}\\ &\quad + \tfrac{1}{\varpi_4}\tilde{\overline{P}}^T\dot{\tilde{\overline{P}}} + \tfrac{1}{\varpi_5}\tilde{\underline{P}}^T\dot{\tilde{\underline{P}}} + \tfrac{1}{\varpi_6}\tilde{C}^T\dot{\tilde{C}}\\ &\quad + \tfrac{1}{\varpi_7}\tilde{B}^T\dot{\tilde{B}} + \tfrac{1}{\varpi_8}\tilde{W}_I^T\dot{\tilde{W}}_I.\end{aligned} \tag{37}$$

Substituting (5) into (37) yields

$$\begin{aligned}\dot{V}_2 &= s\left(\left(\ddot{\theta}_d - bu - f - g - d\right) + \xi_1 m|e|^{m-1}\dot{e} + \xi_2\dot{\delta}(e)\right) + R\\ &= s\left(v + \hat{f} - f - d\right) + R,\end{aligned} \tag{38}$$

where d represents disturbance, and the expression of R is

$$\begin{aligned}R &= \tfrac{1}{\varpi_1}\tilde{W}^T\dot{\tilde{W}} + \tfrac{1}{\varpi_2}\tilde{W}_O^T\dot{\tilde{W}}_O + \tfrac{1}{\varpi_3}\tilde{Q}^T\dot{\tilde{Q}}\\ &\quad + \tfrac{1}{\varpi_4}\tilde{\overline{P}}^T\dot{\tilde{\overline{P}}} + \tfrac{1}{\varpi_5}\tilde{\underline{P}}^T\dot{\tilde{\underline{P}}} + \tfrac{1}{\varpi_6}\tilde{C}^T\dot{\tilde{C}}\\ &\quad + \tfrac{1}{\varpi_7}\tilde{B}^T\dot{\tilde{B}} + \tfrac{1}{\varpi_8}\tilde{W}_I^T\dot{\tilde{W}}_I.\end{aligned}$$

Substituting (15) and parameter learning algorithm (16)–(23) into (38) yields

$$\begin{aligned}\dot{V}_2 &= s\left(v + \hat{f} - f - d\right) + R\\ &= s\Big(-\tfrac{1}{2}\tilde{W}^T\hat{M} - \tfrac{1}{2}\hat{W}^TM_{W_O}\cdot\tilde{W}_O - \tfrac{1}{2}\hat{W}^TM_Q\cdot\tilde{Q}\\ &\quad - \tfrac{1}{2}\hat{W}^TM_{\overline{P}}\cdot\tilde{\overline{P}} - \tfrac{1}{2}\hat{W}^TM_{\underline{P}}\cdot\tilde{\underline{P}} - \tfrac{1}{2}\hat{W}^TM_C\cdot\tilde{C}\\ &\quad - \tfrac{1}{2}\hat{W}^TM_B\cdot\tilde{B} - \tfrac{1}{2}\hat{W}^TM_{W_I}\cdot\tilde{W}_I + v - O_m - d\Big) + R\\ &= s(v - O_m - d).\end{aligned} \tag{39}$$

Substituting (24) and (25) into (39) yields

$$\begin{aligned}\dot{V}_2 &= s(v - O_m - d)\\ &= -\chi_1|s|\left(|s|^{\frac{1}{2}} + \chi_3|s|^{\varphi}\right) - sO_m - sd\\ &\quad - |s|\int\chi_2\left(\tfrac{1}{2} + \chi_3\left(\varphi + \tfrac{1}{2}\right)|s|^{\varphi-1/2} + \chi_3^2\varphi|s|^{2\varphi-1}\right)dt\\ &\le -\chi_1|s|\left(|s|^{\frac{1}{2}} + \chi_3|s|^{\varphi}\right) + |s||O_m| + |s||d|\\ &\quad - |s|\int\chi_2\left(\tfrac{1}{2} + \chi_3\left(\varphi + \tfrac{1}{2}\right)|s|^{\varphi-1/2} + \chi_3^2\varphi|s|^{2\varphi-1}\right)dt\\ &\le |s|\left(-\tfrac{1}{2}\int\chi_2 dt + |O_m| + |d|\right).\end{aligned} \tag{40}$$

According to the properties of the neural network, it is certain that O_m is bounded. Assume that the maximum value of O_m is O_M, and combined with Assumption 2, we can obtain

$$|O_m| + |d| \le O_M + M_D = \Omega,$$

where Ω is an unknown positive number.

Combining (35) and (40) yields

$$\dot{V} = \dot{V}_1 + \dot{V}_2 \le -r_mV_1^{\frac{1}{2}} + \Psi + |s|\left(\Omega - \frac{1}{2}\int_0^t\chi_2 dt\right).$$

Substituting (25)-(27) into (36) yields

$$\Psi = \begin{cases} -|\varepsilon_{\chi_1}|\left(\frac{\pi_1}{\sqrt{2\gamma_1}}\tanh\kappa(|s| - \mu_\chi) - \frac{\pi_1}{\sqrt{2\gamma_1}}\right) - \\ \quad |\varepsilon_{\chi_2}|\left(\frac{\pi_2}{\sqrt{2\gamma_2}}\tanh\kappa(|s| - \mu_\chi) - \frac{\pi_2}{\sqrt{2\gamma_2}}\right), \quad \chi_1 > \chi_\Delta\\ 0, \quad \chi_1 \le \chi_\Delta. \end{cases}$$

The solution for $\tanh\kappa(|s| - \mu_\chi) = \varepsilon_V$ is given by $|s| = \mu = \mu_\chi + \mu_V$,where ε_V is an extremely small positive value and μ_P is a positive value. According to the dynamic changes of s, χ_1, χ_2 and Ω, two potential situations must be taken into account to guarantee the system's stability.

Scenario 1: $|s| > \mu$, $\chi_1 > \chi_\Delta$.

When the value of χ_1 satisfies (32) and χ_2 satisfies $\int_0^t(\chi_2/2)\,dt \ge \Omega$, it can ensure that $\dot{V} \le 0$ holds. If χ_1 and χ_2 do not meet the above two conditions, they will gradually increase according to (25) until both conditions are met. Once the condition that $\dot{V} \le 0$ is met, the system will initiate the convergence process, during which $|s|$ will gradually decline until it reaches the value of $|s| \le \mu$.

Scenario 2: $|s| \le \mu$.

When $\chi_1 > \chi_\Delta$, the value of Ψ is positive. This positivity has the potential to render $\dot{V}$ positive as well. Under such conditions, $|s|$ will progressively exceed μ. At this point, the controller will revert to scenario 1, causing $|s|$ to be drawn back to the level of $|s| \le \mu$. Ultimately, $|s|$ will stabilize in a state where $|s| \le \mu_p$, with μ_p being marginally larger

TABLE II
RJCHRM PHYSICAL PARAMETERS

Parameters	Value	Unit
N	101	-
B_m	0.01	$\mathrm{Nm/rad/sec}$
J_m	0.00051	$\mathrm{kg \cdot m^2}$
J_l	0.00122	$\mathrm{kg \cdot m^2}$
n_p	11	-
K	0.231	$\mathrm{Nm/A}$
$I_{\max}$	5.95	A

than μ. In conclusion, the stability of the system has been demonstrated. To better stabilize s within a small interval, it is necessary to design κ to be sufficiently large. Under this condition, μ is approximately equal to μ_χ , where μ_χ determines the size of the stable interval for s.

Although stability and convergence under arbitrary initial conditions can be theoretically guaranteed under Assumption 1 and Assumption 2, these assumptions may not be strictly satisfied in complex practical systems if controller parameters are poorly designed. Through systematic parameter optimization, steady-state tracking accuracy can be effectively tuned to meet practical requirements. Consequently, the proposed scheme achieves practical stability for the system.

Remark 5: Parameter design rules.

1) Parameter of MFNTSS: Design the relevant parameters according to (6)–(8).
2) Parameters of T2FSHLRNN: The parameters of the novel neural network mainly involve the design of the learning rates. The larger the learning rate, the faster the corresponding parameter evolution. However, an overly large learning rate is prone to over-shooting. The initial values of the remaining parameters can be randomly chosen and subsequently updated online in accordance with equations (16)–(23).
3) Design of variable gains of ATSC: Design the parameters according to (25)-(27). All parameters need to be positive numbers. μ should be chosen to be small enough, as it determines the final convergence range of s.

V. SIMULATION

To validate the efficacy of ATSC-T2FSHLRNN, this research conducts simulation experiments using the Matlab/Simulink platform. The simulation conditions include three types. The parameters of RJCHRM are detailed in Table 2. SMC-RBF [15] and ASTC-RBF [41] are compared. We selected ASTC-RBF and SMC-RBF as comparative methods because they represent a neural-network-enhanced adaptive super-twisting control framework and a classical SMC approach, respectively, comprehensively validating the superior performance of our method in high-precision positioning and mechanical disturbance rejection. Specifically, in SMC-RBF, the RBF neural network serves to approximate the model. To ensure fairness, the optimal parameters are selected for all three controllers, obtained through multiple simulation analyses. The parameters of MFNTSS are $\xi_1 = 2$, $\xi_2 = 2$, $m = 3$, $p = 3$, $q = 5$, and $\Delta_s = 0.01$. The parameters of T2FSHLRNN are $\varpi_1 = 10000$, $\varpi_2 = 0.0001$, $\varpi_3 = 1$, $\varpi_4 = 50$, $\varpi_5 = 50$, $\varpi_6 = 2$, $\varpi_7 = 0.5$, and $\varpi_8 = 0.0001$, $\hat{W}(0) = \begin{bmatrix} 0.1 & 0.1 & 0.1 & 0.1 & 0.1 & 0.1 \end{bmatrix}^T$, $\hat{Q}(0) = \begin{bmatrix} -4 & 0 & 4 \end{bmatrix}^T$, $\hat{\overline{P}}(0) = \begin{bmatrix} 2.5 & 2.5 & 2.5 \end{bmatrix}^T$, $\hat{\underline{P}}(0) = \begin{bmatrix} 1 & 1 & 1 \end{bmatrix}^T$, $\hat{C}(0) = \begin{bmatrix} -3 & 0 & 3 \end{bmatrix}^T$, $\hat{B}(0) = \begin{bmatrix} 3.5 & 3.5 & 3.5 \end{bmatrix}^T$, $\hat{W}_I(0) = \begin{bmatrix} 0.1 & 0.1 & 0.1 \end{bmatrix}^T$, $\hat{W}_O(0) = 0.01$, $exY(0) = 0$, $ex\varphi_1(0) = 1$, $ex\varphi_2(0) = 1$, and $ex\varphi_3(0) = 1$. The parameters of variables gain of ATSC are $\pi_1 = 15$, $\gamma_1 = 5$, $\mu = 0.005$, $\rho = 2$, $\sigma = 1$, $\lambda = 2$, $\chi_\Delta = 1$, $\chi_1(0) = 3$, and $\kappa = 1000$.

TABLE III
PERFORMANCE METRICS OF SINUSOIDAL TRACKING TEST

Controller	SMC-RBF	ASTC-RBF	ATSC-T2FSHLRNN
MAXE	0.0519 rad	0.0547 rad	0.0418 rad
AVERE	0.0049 rad	0.0016 rad	0.0004 rad
RMSE	0.0059 rad	0.0030 rad	0.0020 rad

A. Sinusoidal Tracking Test

The sinusoidal tracking test is used to test the approximation ability of T2FSHLRNN and the dynamic tracking performance of ATSC-T2FSHLRNN. The desired trajectory is $\theta_d = 0.5\pi \sin(0.25\pi t)$. Figs. 5(a)–5(l) show the simulation results.

Fig. 5(a) shows the approximation curve of T2FSHLRNN for the unknown model, and it can be seen that T2FSHLRNN has superior approximation characteristics. Figs. 5(b)–5(i) are the variation diagrams of the adaptive coefficients in T2FSHLRNN. The parameters in the neural network can be automatically optimized online, and they converge within a very short time. Thus, this method is more convenient than methods with fixed base widths and center vectors.

Fig. 5(j) shows the tracking error fluctuation range of ATSC-T2FSHLRNN is ± 0.03 deg, and the curve is smoother compared with those of the other two controllers. To enable a more intuitive comparison of the tracking accuracies of different controllers, MAXE (Maximum Error), AVERE (Average Error), and RMSE (Root Mean Square Error) are used to evaluate the tracking performance, and the calculation results are shown in Table 3. As can be clearly observed from Table 3, the proposed scheme has a more significant fluctuation suppression effect and higher compensation accuracy. The ATSC-T2FSHLRNN control signal (Fig. 5(k)) is the smoothest and most consistent compared to SMC-RBF and ASTC-RBF. This indicates that ATSC-T2FSHLRNN can effectively suppress the chattering of RJCHRM. Although the control signal of ATSC-T2FSHLRNN oscillates significantly in the initial stage, its change is within an acceptable range.

Fig. 5(l) shows the adaptive gain variation of ATSC-T2FSHLRNN. It can be seen that under the influence of interference, s escapes from the boundary μ. At this time, the adaptive gain gradually increases. When s is constrained to satisfy $|s| \leq \mu$, the adaptive gain undergoes monotonic decay. s is always confined within μ_p, which is slightly larger than μ,

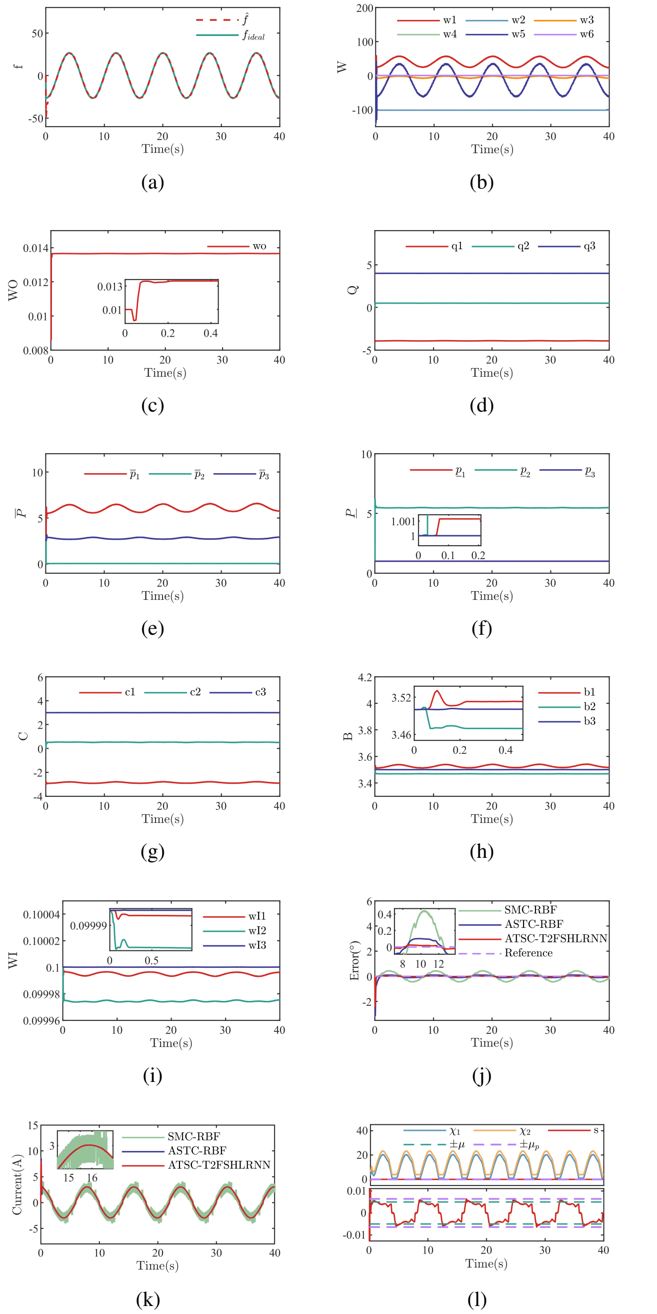

Fig. 5. (a) Effect diagram of T2FSHLRNN; (b) Adaptive curve of W; (c) Adaptive curve of WO; (d) Adaptive curve of Q; (e) Adaptive curve of $\overline{P}$; (f) Adaptive curve of $\underline{P}$; (g) Adaptive curve of C; (h) Adaptive curve of B; (i) Adaptive curve of WI; (j) Tracking error comparison of sinusoidal tracking test; (k) Control law comparison of sinusoidal tracking test; (l) Adaptive gains of ATSC-T2FSHLRNN of sinusoidal tracking test.

and this is consistent with the theoretical analysis in Section IV.B.

B. Dual-sine Tracking Test

To further validate the tracking performance of the proposed control algorithm under complex dynamic conditions, a dual-sine trajectory $\theta_d = 0.5\left(0.5\pi\sin\left(0.25\pi t\right) + 0.5\pi\sin\left(0.5\pi t\right)\right)$ is adopted for simulation verification [44]. All the controller parameters are the same as in the previous test. The simulation results are presented in Figs. 6(a)-6(d).

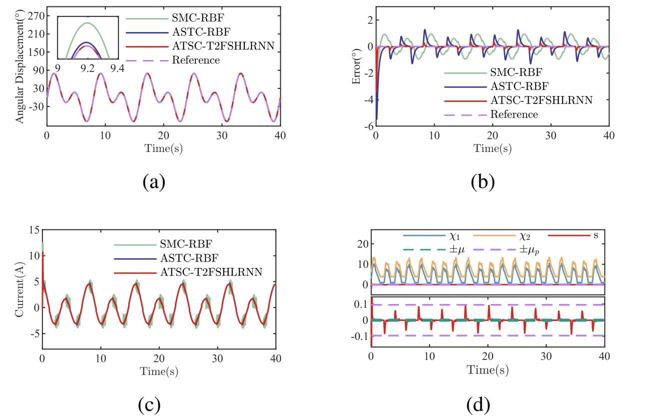

Fig. 6. (a) Tracking performance comparison of dual-sine tracking test;(b) Tracking error comparison of dual-sine tracking test; (c) Control law comparison of dual-sine tracking test; (d) Adaptive gains of ATSC-T2FSHLRNN of dual-sine tracking test.

TABLE IV
PERFORMANCE METRICS OF DUAL-SINE TRACKING TEST

Controller	SMC-RBF	ASTC-RBF	ATSC-T2FSHLRNN
MAXE	0.0818 rad	0.0956 rad	0.0598 rad
AVERE	0.0087 rad	0.0052 rad	0.0008 rad
RMSE	0.0105 rad	0.0099 rad	0.0031 rad

As shown in Fig. 6(a) and Fig. 6(b), the ATSC-T2FSHLRNN can effectively track the double sinusoidal trajectory, with its tracking error significantly smaller than the other two controllers. Fig. 6(c) presents the comparison of control laws, where the SMC-RBF still exhibits strong chattering, while the other two controllers remain relatively stable. Fig. 6(d) displays the adaptive gains of ATSC-T2FSHLRNN. It can be observed that under the combined effect of dual-frequency sinusoidal signals, the amplitude of s exceeding the boundary is 0.1 deg, which is notably larger than that in the single sinusoidal tracking scenario. After s exceeds the boundary, the adaptive gain mechanism actively drives it back to $|s| \leq \mu$. Comparative performance metrics are presented in Table 4. The above analysis and Table 4 demonstrate that the ATSC-T2FSHLRNN can successfully accomplish the dual sinusoidal curve tracking task.

C. Step and Disturbance Rejection Test

The step and disturbance rejection test is used to evaluate the transient response performance and disturbance rejection

TABLE V
PERFORMANCE METRICS OF STEP AND DISTURBANCE REJECTION TEST

Controller	SMC-RBF	ASTC-RBF	ATSC-T2FSHLRNN
MAXE	0.000925 rad	0.000628 rad	0.000471 rad
AVERE	0.000070 rad	0.000035 rad	0.000009 rad
RMSE	0.000157 rad	0.000105 rad	0.000047 rad

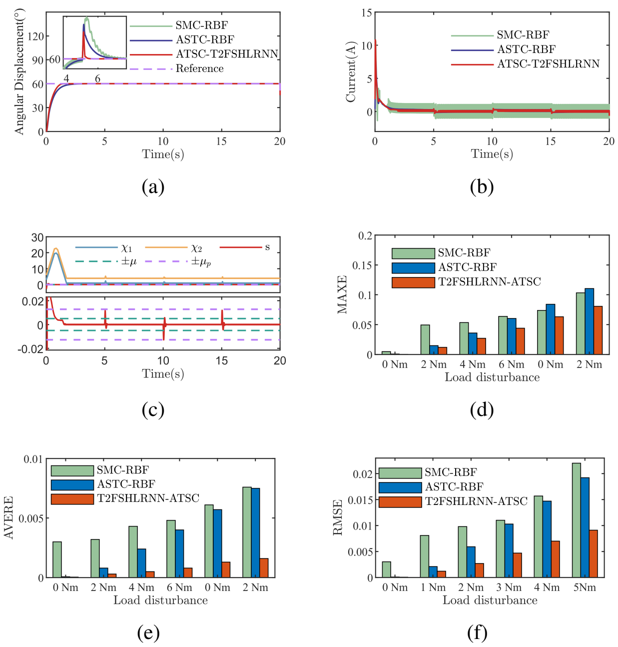

Fig. 7. (a) Tracking error comparison of step and disturbance rejection test; (b) Control law comparison of step and disturbance rejection test; (c) Adaptive gains of ATSC-T2FSHLRNN of step and disturbance rejection test; (d MAXE values under different load disturbances; (e) AVERE values under different load disturbances; (f) RMSE values under different load disturbances.

ability of the ATSC-T2FSHLRNN. The desired value of the signal is $\theta_d = \pi/3\,\mathrm{rad}$. The disturbance signal is a square-wave signal applied at the load end, with an amplitude of 2 Nm, a period of 10 seconds, and a duty cycle of 50%. The parameters are the same as before. Figs. 7(a)–7(c) show the simulation results.

It can be seen from Fig. 7(a) that the ATSC-T2FSHLRNN can quickly track the desired signal. The time required to reach the steady state is approximately 1.8 s, which is notably quicker than that of the other two control methods. We use MAXE, AVERE, and RMSE during the steady-state phase to evaluate the tracking performance, and results are presented in Table 5. The ATSC-T2FSHLRNN exhibits more outstanding transient response performance.

Among three controllers, ATSC-T2FSHLRNN generates the most stable control input (Fig. 7(b)). This finding suggests that ATSC-T2FSHLRNN effectively mitigates system chattering, thereby averting potential damage to the actuator. Moreover, it validates the non-singularity of the proposed controller. Although the control signal of the ATSC-T2FSHLRNN undergoes a more pronounced change in the initial phase compared to the other two controllers, the magnitude of this change remains within an acceptable threshold. This phenomenon is in line with the faster convergence rate of ATSC-T2FSHLRNN. Fig. 7(d) presents the adaptive gains of ATSC-T2FSHLRNN. The variation in the adaptive gains is consistent with the outcomes of the sinusoidal tracking test, further corroborating the theoretical analysis presented in Section IV.B.

Upon the application of load torque, distinct abrupt variations emerge in the tracking curves of the three controllers. Notably, the amplitude of such variations in ATSC-T2FSHLRNN is relatively smaller. Subsequently, the tracking trajectory of ATSC-T2FSHLRNN rapidly converges to steady state, demonstrating significantly faster response compared to the other two controllers. The abrupt changes in the adaptive gain curve align precisely with the transitions of the square-wave signal (Fig. 7(c)). As shown in Fig. 7(b), the robustness of the SMC-RBF is achieved through control inputs with high-amplitude and high-frequency switching characteristics. After reaching the steady state, both inputs of ASTC-RBF and ATSC-T2FSHLRNN exhibit extremely narrow fluctuation ranges.

Furthermore, we set the load disturbance torque at 0 Nm, 1 Nm, 2 Nm, 3 Nm, 4 Nm, and 5 Nm and conducted multiple repeated experiments. Subsequently, the average values of the performance metrics were calculated. To facilitate a visual comparison of the tracking performance, these metrics are presented in the form of a histogram in Figs. 7(d)–7(f). ATSC-T2FSHLRNN quantitatively performs better than SMC-RBF and ASTC-RBF on all three metrics. The above simulation results indicate that ATSC-T2FSHLRNN significantly outperforms the other two controllers in terms of tracking accuracy, response speed, anti-interference ability, and chattering suppression.

VI. Conclusion

In this article, an ATSC-T2FSHLRNN is presented for robot joints. An MFNTSS is devised to avoid singularity and accelerate the convergence rate of SMC. To tackle the uncertain modeling of robot joints, a T2FSHLRNN is introduced. Variable gains are designed to ensure system stability under unknown disturbances. Simulation results verify the proposed method's steady-state and transient tracking performance and disturbance rejection capability. In future research, experiments will be conducted to further validate the ATSC-T2FSHLRNN's effectiveness.

References

[1] J. Zhao and T. Iwasaki, "CPG Control for Harmonic Motion of Assistive Robot With Human Motor Control Identification," *IEEE Transactions on Control Systems Technology*, vol. 28, no. 4, pp. 1323-1336, Jul. 2020.

[2] Q. Wang *et al.*, "Hysteresis identification of joint with harmonic drive transmission based on Monte Carlo method," *Mechatronics*, vol. 99, May 2024, Art. no. 103166.

[3] C. Wang, Y. Zhuang, J. Yang, Y. Liu, and J. Pan, "Characteristic Analysis and Control Loop Design of Transmission Torque and Jerk for Flexible Joint Servo Systems," *IEEE Transactions on Power Electronics*, vol. 39, no. 7, pp. 8528-8539, Jul. 2024.

[4] Q. Zhang and G. Liu, "Precise Control of Elastic Joint Robot Using an Interconnection and Damping Assignment Passivity-Based Approach," *IEEE/ASME Transactions on Mechatronics*, vol. 21, no. 6, pp. 2728-2736, Dec. 2016.

[5] F. Petit, A. Daasch, and A. Albu-Schäffer, "Backstepping Control of Variable Stiffness Robots," *IEEE Transactions on Control Systems Technology*, vol. 23, no. 6, pp. 2195-2202, Nov. 2015.

[6] Y. Pan, H. Wang, X. Li, and H. Yu, "Adaptive Command-Filtered Backstepping Control of Robot Arms With Compliant Actuators," *IEEE Transactions on Control Systems Technology*, vol. 26, no. 3, pp. 1149-1156, May 2018.

[7] Y. Shi, Y. Yu, H. Li, B. Han, X. Liu, and X. Chen, "Speed Fluctuation Suppression by Model-Based Feed-Forward Control in Gimbal System With Harmonic Drive," *IEEE Transactions on Power Electronics*, vol. 37, no. 6, pp. 6678-6687, Jun. 2022.

[8] J. Kim and E. A. Croft, "Full-State Tracking Control for Flexible Joint Robots With Singular Perturbation Techniques," *IEEE Transactions on Control Systems Technology*, vol. 27, no. 1, pp. 63-73, Jan. 2019.

[9] S. Zhen, X. Peng, X. Liu, H. Li, and Y.-H. Chen, “A new PD based robust control method for the robot joint module,” *Mechanical Systems and Signal Processing*, vol. 161, Dec. 2021, Art. no. 107958.

[10] X. Chen, H. Zhao, and J. Cheng, “Robust Controller Design for Robot Joint Motor Modules Based on Dynamical Model,” *IEEE Transactions on Applied Superconductivity*, vol. 34, no. 8, pp. 1-5, Nov. 2024.

[11] M. Ali and H. Mirinejad, “Robust tracking control of flexible manipulators using hybrid backstepping/nonlinear reduced-order active disturbance rejection control,” *ISA Transactions*, vol. 149, pp. 229-236, Jun. 2024.

[12] S. Diao, W. Sun, S. F. Su, X. Zhao, and N. Xu, “Novel Adaptive Control for Flexible-Joint Robots With Unknown Measurement Sensitivity,” *IEEE Transactions on Automation Science and Engineering*, vol. 21, no. 2, pp. 1445-1456, Apr. 2024.

[13] E. Kelekci and S. Kizir, “Trajectory and vibration control of a flexible joint manipulator using interval type-2 fuzzy logic,” *ISA Transactions*, vol. 94, pp. 218-233, Nov. 2019.

[14] D. Shang, X. Li, M. Yin, and F. Li, “Dynamic modeling and fuzzy adaptive control strategy for space flexible robotic arm considering joint flexibility based on improved sliding mode controller,” *Advances in Space Research*, vol. 70, no. 11, pp. 3520-3539, Dec. 2022.

[15] H. Li, S. Yang, L. Kong, and T. Wen, “High-Precision Angular Speed Tracking Control of Gimbal System With Harmonic Reducer,” *IEEE Transactions on Industrial Electronics*, vol. 69, no. 8, pp. 8168-8177, Aug. 2022.

[16] Q. Zhang et al., “An adaptive type-2 fuzzy sliding mode tracking controller for a robotic manipulator,” *era*, vol. 31, no. 7, Art. no. era-31-07-193, 2023.

[17] H. Rahali, S. Zeghlache, B. D. E. Cherif, L. Benyettou, and A. Djerioui, “Robust adaptive fuzzy type-2 fast terminal sliding mode control of robot manipulators in attendance of actuator faults and payload variation,” *Electrical Engineering & Electromechanics*, no. 1, Art. no. 1, Jan. 2025.

[18] R. Amar, H. Mustapha, and T. Mohamed, “Decentralized RBFNN Type-2 Fuzzy Sliding Mode Controller for Robot Manipulator Driven by Artificial Muscles,” *International Journal of Advanced Robotic Systems*, vol. 9, no. 5, p. 182, Nov. 2012.

[19] D. Zholtayev, M. Rubagotti, and T. D. Do, “Adaptive super-twisting sliding mode control for maximum power point tracking of PMSG-based wind energy conversion systems,” *Renewable Energy*, vol. 183, pp. 877-889, Jan. 2022.

[20] K. Zhao *et al.*, “Robust model-free super-twisting sliding-mode control method based on extended sliding-mode disturbance observer for PMSM drive system,” *Control Engineering Practice*, vol. 139, Oct. 2023, Art. no. 105657.

[21] X. Xiong, X. Xiang, Q. Zhang, and S. Yang, “Adaptive super-twisting control of underwater intervention system considering dynamic couplings and uncertainties,” *IET Control Theory & Applications*, vol. 17, no. 13, pp. 1813–1829, 2023.

[22] J. Fei and L. Liu, “Fuzzy Neural Super-Twisting Sliding-Mode Control of Active Power Filter Using Nonlinear Extended State Observer,” *IEEE Transactions on Systems, Man, and Cybernetics: Systems*, vol. 54, no. 1, pp. 457–470, Jan. 2024.

[23] Y. Xia et al., “Customized Non-Monotonic Prescribed Performance Control for Stochastic MEMS Gyroscopes With Insufficient Input Capability,” *IEEE Transactions on Circuits and Systems I: Regular Papers*, pp. 1–13, 2025.

[24] J. Yuan, N. Qi, Z. Qiu, and F. Wang, “Adaptive RBF observer-sliding mode controller design for a two dimensional aeroelastic system with unsteady aerodynamics,” *Aerospace Science and Technology*, vol. 80, pp. 482-495, Sep. 2018.

[25] N. M. Moawad, W. M. Elawady, and A. M. Sarhan, “Development of an adaptive radial basis function neural network estimator-based continuous sliding mode control for uncertain nonlinear systems,” *ISA Transactions*, vol. 87, pp. 200-216, Apr. 2019.

[26] A. Zhai, H. Zhang, J. Wang, G. Lu, J. Li, and S. Chen, “Adaptive neural synchronized impedance control for cooperative manipulators processing under uncertain environments,” *Robotics and Computer-Integrated Manufacturing*, vol. 75, p. 102291, Jun. 2022.

[27] J. Liu, *Radial Basis Function (RBF) Neural Network Control for Mechanical Systems: Design, Analysis and Matlab Simulation*. Berlin, Heidelberg: Springer, 2013.

[28] J. Fei and C. Lu, “Adaptive Sliding Mode Control of Dynamic Systems Using Double Loop Recurrent Neural Network Structure,” *IEEE Transactions on Neural Networks and Learning Systems*, vol. 29, no. 4, pp. 1275-1286, Apr. 2018.

[29] Y. Chu, J. Fei, and S. Hou, “Adaptive Global Sliding-Mode Control for Dynamic Systems Using Double Hidden Layer Recurrent Neural Network Structure,” *IEEE Transactions on Neural Networks and Learning Systems*, vol. 31, no. 4, pp. 1297-1309, Apr. 2020.

[30] S. C. Yogi, V. K. Tripathi, and L. Behera, “Adaptive Integral Sliding Mode Control Using Fully Connected Recurrent Neural Network for Position and Attitude Control of Quadrotor,” *IEEE Transactions on Neural Networks and Learning Systems*, vol. 32, no. 12, pp. 5595–5609, Dec. 2021.

[31] R. J. Wai and R. Muthusamy, “Fuzzy-Neural-Network Inherited Sliding-Mode Control for Robot Manipulator Including Actuator Dynamics,” *IEEE Transactions on Neural Networks and Learning Systems*, vol. 24, no. 2, pp. 274-287, Feb. 2013.

[32] M. Abudusaimaiti, A. Abdurahman, H. Jiang, and C. Hu, “Fixed/predefined-time synchronization of fuzzy neural networks with stochastic perturbations,” *Chaos, Solitons & Fractals*, vol. 154, Jan. 2022, Art. no. 111596.

[33] Y. Xia, J. He, H.-K. Lam, L. Rutkowski, and R.-E. Precup, “Non-fragile fuzzy control of input-saturated systems with global prescribed performance via an error-triggered mechanism,” *Information Sciences*, vol. 711, p. 122111, Sep. 2025.

[34] Z. Zhou and B. Wu, “Adaptive sliding mode control of manipulators based on fuzzy random vector function links for friction compensation,” *Optik*, vol. 227, p. 166055, Feb. 2021.

[35] S. Hou, J. Fei, C. Chen, and Y. Chu, “Finite-Time Adaptive Fuzzy-Neural-Network Control of Active Power Filter,” *IEEE Transactions on Power Electronics*, vol. 34, no. 10, pp. 10298–10313, Oct. 2019.

[36] Z. Wang and J. Fei, “Fractional-Order Terminal Sliding-Mode Control Using Self-Evolving Recurrent Chebyshev Fuzzy Neural Network for MEMS Gyroscope,” *IEEE Transactions on Fuzzy Systems*, vol. 30, no. 7, pp. 2747-2758, Jul. 2022.

[37] M. H. Hamedani, M. Zekri, F. Sheikholeslam, M. Selvaggio, F. Ficuciello, and B. Siciliano, “Recurrent fuzzy wavelet neural network variable impedance control of robotic manipulators with fuzzy gain dynamic surface in an unknown varied environment,” *Fuzzy Sets and Systems*, vol. 416, pp. 1-26, Jul. 2021.

[38] J. Fei, Y. Chen, L. Liu, and Y. Fang, “Fuzzy Multiple Hidden Layer Recurrent Neural Control of Nonlinear System Using Terminal Sliding-Mode Controller,” *IEEE Transactions on Cybernetics*, vol. 52, no. 9, pp. 9519–9534, Sep. 2022.

[39] S. Hou, Y. Chu, and J. Fei, “Adaptive Type-2 Fuzzy Neural Network Inherited Terminal Sliding Mode Control for Power Quality Improvement,” *IEEE Transactions on Industrial Informatics*, vol. 17, no. 11, pp. 7564–7574, Nov. 2021.

[40] J. Wang, L. Zhao, and L. Yu, “Adaptive Terminal Sliding Mode Control for Magnetic Levitation Systems With Enhanced Disturbance Compensation,” *IEEE Transactions on Industrial Electronics*, vol. 68, no. 1, pp. 756-766, Jan. 2021.

[41] B. Kumar, S. K. Swain, S. K. Mishra, Y. K. Singh, and S. Ghosh, “Radial Basis Function-based Adaptive Gain Super-Twisting Controller for Magnetic Levitation System with Time-Varying External Disturbance,” *IEEE Transactions on Transportation Electrification*, vol. 10, no. 4, pp. 9121-9132, Dec. 2024.

[42] Q. Hou, S. Ding, and X. Yu, “Composite Super-Twisting Sliding Mode Control Design for PMSM Speed Regulation Problem Based on a Novel Disturbance Observer,” *IEEE Transactions on Energy Conversion*, vol. 36, no. 4, pp. 2591-2599, Dec. 2021.

[43] Q. Hou and S. Ding, “GPIO Based Super-Twisting Sliding Mode Control for PMSM,” *IEEE Transactions on Circuits and Systems II: Express Briefs*, vol. 68, no. 2, pp. 747-751, Feb. 2021.

[44] S. Ling, H. Wang, and P. X. Liu, “Adaptive fuzzy dynamic surface control of flexible-joint robot systems with input saturation,” IEEE/CAA Journal of Automatica Sinica, vol. 6, no. 1, pp. 97–107, Jan. 2019.

Xiao Lin (Member IEEE) received the M.S. degree from School of Automotive Engineering, Dalian University of Technology, Dalian, China, in 2014. He is currently pursuing a Ph.D. degree in the School of Mechanical Engineering and Vehicle Engineering at Chongqing University. His areas of interest include nonlinear control systems, artificial intelligence and machine learning.

Yu Xia (Member IEEE) received his Ph.D. degree in mechanical engineering from Chongqing University, Chongqing, China, in 2024. He is currently a Research Fellow in the State Key Laboratory of Mechanical System and Vibration, School of Mechanical Engineering, Shanghai Jiao Tong University, Shanghai, China. His research interests include prescribed performance control, stochastic system control, and electromechanical system control.

Zsófia Lendek (Member IEEE) received the M.Sc. degree in control engineering from the Technical University of Cluj-Napoca, Romania, in 2003, the Ph.D. degree from the Delft University of Technology, the Netherlands, in 2009, and her habilitation degree from the Technical University of Cluj-Napoca, Romania, in 2019. She is currently a Full Professor at the Technical University of Cluj-Napoca, Romania. She has previously held research positions in the Netherlands and in France. Her research interests include observer and controller design for nonlinear systems, in particular Takagi-Sugeno fuzzy systems, which adapt the advantages of linear time-invariant system-based design to nonlinear systems, with applications in several fields.

Dr. Lendek is an Associate Editor of IEEE TRANSACTIONS ON FUZZY SYSTEMS and *Engineering Applications of Artificial Intelligence*, and an Editorial Board Member of *Fuzzy Sets and Systems*.

Radu-Emil Precup (Fellow, IEEE) received the Dipl.Ing. (with honors) degree in automation and computers from the "Traian Vuia" Polytechnic Institute of Timisoara, Timisoara, Romania, the Dipl. degree in mathematics from the West University of Timisoara, Timisoara, and the Ph.D. degree in automatic systems from the Politehnica University of Timisoara (UPT), Timisoara, Romania, in 1987, 1993, and 1996, respectively. He is currently with UPT, Timisoara, Romania, where he became a Professor with the Department of Automation and Applied Informatics in 2000. From 2022, he is also a senior researcher (CS I) and the head of the Data Science and Engineering Laboratory of the Center for Fundamental and Advanced Technical Research, Romanian Academy – Timisoara Branch, Romania. From 2016 to 2022, he was an Adjunct Professor within the School of Engineering, Edith Cowan University, Joondalup, WA, Australia. He is the author or co-author of more than 300 papers. His current research interests include intelligent and data-driven control systems.

Prof. Precup is a corresponding member of the Romanian Academy, and a member of the Technical Committees on Data-Driven Control and Monitoring, and Control, Robotics and Mechatronics of the IEEE Industrial Electronics Society. He is the Editor-in-Chief of *Romanian Journal of Information Science and Technology*, a Senior Editor of IEEE Open Journal of the Computer Society, and an Associate Editor of IEEE TRANSACTIONS ON CYBERNETICS and IEEE TRANSACTIONS ON NEURAL NETWORKS AND LEARNING SYSTEMS.

Imre J. Rudas (Life Fellow, IEEE) received the bachelor's degree in mechanical engineering from Bànki Donát Polytechnic College, Budapest, Hungary, in 1971. He received the master's degree in mathematics from Eötvös Loránd University, Budapest, Hungary, in 1977, the Ph.D. degree in robotics and the Doctor of Science degree in computer science from the Hungarian Academy of Sciences, Budapest, in 1987 and 2004, respectively, and the Doctor Honoris Causa degrees in computer science from the Technical University of Košice, Košice, Slovakia, in 2001; the Politehnica University of Timișoara, Timișoara, Romania, in 2005; Óbuda University, Budapest, Hungary, in 2014; and the Slovak University of Technology in Bratislava, Bratislava, Slovakia, in 2016.

He is a Rudolf Kalman Distinguished Professor, a Rector Emeritus, and a Professor Emeritus with Óbuda University, Budapest. He has edited and/or published 22 books, published more than 890 papers in international scientific journals, conference proceedings, and book chapters, and received more than 8000 citations. His present areas of research activities are Computational Cybernetics, Cyber Physical Control, Robotics, and Systems of Systems.

Dr. Rudas was awarded the Honorary Professor Title in 2013 and the Ambassador Title by the Wrocław University of Science and Technology. He is the Senior Past President of the IEEE Systems, Man, and Cybernetics Society. He is a Fellow of the International Fuzzy Systems Association.

Ramesh K. Agarwal (Life Fellow, IEEE) received the Ph.D. degree in aerospace engineering from Stanford University, Stanford, CA, USA, in 1975. He is currently the William Palm Professor of engineering and the Director of the Aerospace Research and Education Center, Washington University in St. Louis, St. Louis, MO, USA. He has authored or coauthored more than 500 journal and refereed conference articles. His research interests include basic control system theory, fuzzy logic and neural networks, and applications of nonlinear H_∞ control to flight and flow control. He was on the editorial board for more than 20 journals. He was the recipient of the SAE Aerospace Engineering Leadership Award in 2013, the SAE Excellence in Engineering Education Award, the SAE International Medal of Honor, and the AIAA Reed Aeronautics Award in 2015. He is a Fellow of AAAS, AIAA, APS, ASME, and IET.